

UPCommons

Portal del coneixement obert de la UPC

<http://upcommons.upc.edu/e-prints>

Aquesta és la versió revisada per parells del següent article:

Ventosa, J. [et al] (2016) Numerical analysis of conservative unstructured discretisations for low Mach flows. " International journal for numerical methods in fluids". Doi: 10.1002/fld.4350,

la qual ha estat publicada en la versió definitiva a <http://dx.doi.org/10.1002/fld.4350>.

Aquest article pot ser utilitzat per a fins no comercials, d'acord amb els [termes i condicions d'auto-arxiu de Wiley](#).

This is the peer reviewed version of the following article:

Ventosa, J. [et al] (2016) Numerical analysis of conservative unstructured discretisations for low Mach flows. " International journal for numerical methods in fluids". Doi: 10.1002/fld.4350,

which has been published in final form at <http://dx.doi.org/10.1002/fld.4350>.

This article may be used for non-commercial purposes in accordance with [Wiley Terms and Conditions for Self-Archiving](#).

Numerical analysis of conservative unstructured discretisations for low Mach flows

J. Ventosa-Molina¹, J. Chiva¹, O. Lehmkuhl^{1,2}, J. Muela¹, C. D. Pérez-Segarra¹ and A. Oliva^{1,*,\dagger}

¹*Centre Tecnològic de Transferència de Calor (CTTC), Universitat Politècnica de Catalunya-BarcelonaTech (UPC), ESEIAAT,*

Colom 11, Terrassa, Barcelona 08222, Spain

²*Termo Fluids, S.L. Av. Jacquard, 97 1-E, Terrassa, Barcelona 08222, Spain*

SUMMARY

Unstructured meshes allow easily representing complex geometries and to refine in regions of interest without adding control volumes in unnecessary regions. However, numerical schemes used on unstructured grids have to be properly defined in order to minimise numerical errors. An assessment of a low Mach algorithm for laminar and turbulent flows on unstructured meshes using collocated and staggered formulations is presented. For staggered formulations using cell-centred velocity reconstructions, the standard first-order method is shown to be inaccurate in low Mach flows on unstructured grids. A recently proposed least squares procedure for incompressible flows is extended to the low Mach regime and shown to significantly improve the behaviour of the algorithm. Regarding collocated discretisations, the odd–even pressure decoupling is handled through a kinetic energy conserving flux interpolation scheme. This approach is shown to efficiently handle variable-density flows. Besides, different face interpolations schemes for unstructured meshes are analysed. A kinetic energy-preserving scheme is applied to the momentum equations, namely, the symmetry-preserving scheme. Furthermore, a new approach to define the far-neighbouring nodes of the quadratic upstream interpolation for convective kinematics scheme is presented and analysed. The method is suitable for both structured and unstructured grids, either uniform or not. The proposed algorithm and the spatial schemes are assessed against a function reconstruction, a differentially heated cavity and a turbulent self-igniting diffusion flame. It is shown that the proposed algorithm accurately represents unsteady variable-density flows. Furthermore, the quadratic upstream interpolation for convective kinematics scheme shows close to second-order behaviour on unstructured meshes, and the symmetry-preserving is reliably used in all computations.

KEY WORDS: low Mach; segregated algorithm; unstructured; collocated; staggered; reacting flows

1. INTRODUCTION

Numerical algorithms to simulate low Mach number flows have received increasing attention over the past decades because they apply to a wide range of applications, such as natural phenomena or in technological designs. A further issue to consider is that in most cases the flows of interest are turbulent, which require stable and accurate algorithms. Combustion processes, meteorological flows and solar energy are examples of their applicability. The low Mach number approximation of the Navier–Stokes equations is characterised by being able to handle flows with a Mach number much lower than unity ($Ma \ll 1$) but with strong density variations. Large temperature or concentration

*Correspondence to: Assensi Oliva, Centre Tecnològic de Transferència de Calor (CTTC), Universitat Politècnica de Catalunya-BarcelonaTech (UPC), ESEIAAT, Colom 11, Terrassa, Barcelona 08222, Spain.

[†]E-mail: cttc@cttc.upc.edu

gradients may be the cause for them. These high variations in density do not correspond to high pressure variations within the flow, which in fact are low.

Despite having similar ranges of applicability, incompressible algorithms, which make use of the Boussinesq approximation, are not suitable when temperature variations are higher than 10% around the mean, as shown by Gray and Giorgini [1]. On the other hand, compressible formulations of the Navier–Stokes equations are suited to study flows with strong density variations. However, at low Mach numbers, standard explicit compressible algorithms present stability issues resulting in strong time-step limitations. These limitations are imposed by numerical requirements, namely, the Courant–Friedrich–Lewy condition, as the acoustic phenomena implicit in the compressible equations must be accounted for.

Two different approaches are found in the literature to deal with variable density flows at low Mach numbers. On the one hand, extensions of explicit compressible algorithms, in which usually a preconditioner is applied. These algorithms are commonly referred as ‘all Mach flows’. On the other hand, at low Mach numbers, when acoustic phenomena is not of interest, high-order dependencies on the Mach number of the Navier–Stokes equations can be filtered out. Consequently, the formulation is not restricted by the Mach number. These methods usually employ similar strategies as incompressible formulations and therefore are commonly denoted as ‘pressure based’ or ‘segregated algorithms’. The algorithm employed in the current study falls in the latter category

The literature is rich in algorithms to solve low Mach flows using either strategy. Regarding ‘all Mach flows’, most algorithms use a preconditioning strategy, which is not easily defined, in order to overcome the stiffness of compressible algorithms at low Mach numbers, see references [2–5] and references therein for some examples. Concerning ‘pressure-based’ algorithms, De Sampaio and Moreira [6] and Becker and Braack [7] used the low Mach number approximation and solved the system of equations by means of a finite element approaches. Darbandi and Hosseinizadeh [8] proposed a modification to the incompressible semi-implicit method for pressure linked equations algorithm in finite-volume formulations to account for large density variations. Similarly, Lien [9] proposed a modification of the semi-implicit method for pressure linked equations algorithm applied to all-speed flows on unstructured meshes. Shunn *et al.* [10] studied a semi-implicit fractional step using structured and unstructured finite-volume meshes. Najm *et al.* [11] proposed a low Mach algorithm based on the classical fractional step of Kim and Moin [12] in a finite-volume approach. Similarly, Nicoud [13], Knikker [14] and Lessani and Papalexandris [15] proposed approaches in a finite difference context.

Regarding the spatial discretisation, most of the studies cited reported structured/Cartesian meshes [3, 8, 11, 13–17]. Use of structured meshes is suitable for simple geometries, but more complex ones are better handled using unstructured grids. Furthermore, this framework is of interest for industrial applications, where, because of the complex designs, use of unstructured meshes reduces the computational requirements or becomes a must if the geometry is very complex. Still, different algorithms using unstructured meshes have been proposed. Vierendeels *et al.* analysed a low Mach algorithm on highly distorted structured meshes [18, 19]. Staggered approaches using covolume meshes, which require Delaunay–Voronoi meshes, have been proposed and successfully used [20]. However, construction of such meshes is not straightforward. Extension to arbitrary unstructured meshes using staggered approaches but for incompressible flows has also been considered [21, 22]. Concerning collocated schemes, Lien [9] proposed a segregated algorithm for all-speed flows, Mahesh *et al.* initially developed an scheme for incompressible flows on complex geometries [23] and later extended it to the variable density case [24], and Shunn *et al.* [10] using a similar approach, proposed a verification process for low Mach algorithms where unstructured meshes were used.

In the context of the finite-volume method, collocated or staggered discretisations are used to handle the pressure-velocity coupling. Collocated and staggered approaches differ in the location of the momentum’s primary variables, velocity and pressure. In the collocated formulation, both pressure and velocity are placed at cell centres, while in the staggered formulation, velocity is placed at cell faces and pressure at cell centres. This staggering of the velocity requires the construction of a displaced mesh around cells’ faces in order to perform the temporal integration. The collocated approach is preferred in complex grids as it is not required to construct these displaced meshes. However, the collocated formulation presents an *odd–even decoupling* between pressure and veloc-

ity, which the staggered formulation does not manifest. Felten and Lund [25] proposed a mass flux correction in order to avoid this pressure-velocity decoupling for incompressible flows and a mass flux interpolation scheme in order to minimise kinetic energy preservation errors because of the pressure gradient. As for the staggered discretisation, the cost is then the construction of a suitably displaced mesh, which in Cartesian meshes is easily performed. However, in body-fitted or unstructured meshes, it is not as straightforward. Nonetheless, Perot [26] proposed an effortless method to construct a displaced grid on unstructured meshes. Still, this method relies on the computation of the cell-centred velocities.

Aside from defining a framework to tackle the pressure-velocity coupling suitable to be used on unstructured meshes, attention must also be given to the numerical interpolations. Many different schemes have been proposed in the literature, that is, upwinding schemes, centred approximations and flux limiter schemes. Their suitability is assessed in terms of numerical accuracy and stability. Notwithstanding, in the context of the momentum equations, the importance of numerically preserving kinetic energy been shown by several authors [23, 25, 27–29] to be a critical aspect in terms of numerical stability. To this end, the symmetry-preserving (SP) scheme is applied to the momentum equations throughout this work and its suitability to yield accurate results studied.

Still, in transport equations of scalars, such as the temperature, this requirement of kinetic energy preservation is not placed and the former criteria of accuracy and stability prevails. In this context, it is of interest to use high-order interpolation schemes. In structured meshes, high-order schemes are usually easily devised, and their viability is mostly limited by stability aspects. However, as it can readily be seen in Segarra *et al.* [30], in the process of devising high-order schemes for unstructured meshes, low-order intermediate approximations must be made, thus affecting their theoretical high-order properties. Non-orthogonal effects and the difficulties in defining high-order stencils for a given interpolation hinder the possibility of constructing high-order schemes.

In order to analyse the challenges described, in this paper, both Felten and Lund's collocated and Perot's staggered formulations are extended to the variable density case in the context of a pressure based algorithm, namely, a fractional step method. The cell-centred flux correction proposed by Felten and Lund [25] for incompressible flows is extended to variable density flows and shown to correctly describe the fluid flow. Regarding the staggered discretisation, the first-order cell-centred velocity proposed by Perot [26] is analysed alongside a recently proposed second-order velocity reconstruction proposed by Jofre *et al.* [29]. Additionally, the accuracy of face interpolation schemes in unstructured grids is also assessed. Furthermore, aiming at developing a suitable algorithm to handle turbulent flows the SP discretisation is applied to the momentum equations, and it is shown to provide accurate results.

In order to cover all aspects related to the modelling of low Mach flows the paper is organised as follows. In Section 2, the low Mach equations are presented for both non-reacting and reacting cases. Following, in Section 3, the pressure-velocity coupling is described together with the fractional step method used to solve it. In Section 4, two different numerical frameworks are presented to discretise the differential equations. Both collocated and staggered methods are described in the context of the momentum equation. Furthermore, at the end of the section, different face interpolation for the convective term are described. Next, in Section 5, the temporal integration algorithm is described. Focus is placed to the differences between using collocated or staggered approaches. The numerical analysis is shown in Section 6. Three tests have been performed in order to analyse the different discretisations and numerical schemes. In the first one, the numerical interpolations are tested on unstructured meshes by performing a reconstruction of an analytical function. In the second one, both collocated and staggered formulations are studied using a non-reacting laminar test case, namely, a differentially heated square cavity filled with air under a large temperature difference [31]. This test also serves as verification of the coupled behaviour of numerical interpolations and spatial formulations. In the third test case, the full algorithm is tested against a transient turbulent chemically reacting flow, consisting in the auto-ignition of a hydrogen jet flowing into a hot air coflow, based on the experiments of Markides and Mastorakos [32]. This case serves to ascertain the correct transient behaviour of the proposed algorithm and the capability of the spatial schemes to handle variable density flows in the turbulent regime. Finally, in the conclusions, the main findings of the present study are gathered.

2. LOW MACH NUMBER EQUATIONS

In order to obtain the low Mach number approximation to the Navier–Stokes equations, these equations are taken in their compressible form, and the Mach dependent variables are expanded in power series of the ratio of the dynamic to the thermodynamic pressure [15, 21], which is a measure of the compressibility effects. For flows at low Mach numbers here considered, this is a small parameter. Thus, keeping the lowest-order terms of this expansion, the low Mach number equations are

$$\frac{\partial \rho}{\partial t} = -\frac{\partial \rho u_j}{\partial x_j} \quad (1)$$

$$\frac{\partial \rho u_i}{\partial t} = -\frac{\partial \rho u_j u_i}{\partial x_j} - \frac{\partial p}{\partial x_i} + \frac{\partial \tau_{ij}}{\partial x_j} + \rho g_i \quad (i = 1, 2, 3) \quad (2)$$

$$\rho \frac{\partial h}{\partial t} = -\rho u_j \frac{\partial h}{\partial x_j} + \frac{dP_o}{dt} - \frac{\partial \dot{q}_j}{\partial x_j}, \quad (3)$$

where $\tau_{ij} = \mu \left(\frac{\partial u_i}{\partial x_j} + \frac{\partial u_j}{\partial x_i} - \frac{2}{3} \delta_{ij} \frac{\partial u_k}{\partial x_k} \right)$ and $\dot{q}_j = -\kappa \frac{\partial T}{\partial x_j}$. In the momentum equation, p may be interpreted as the hydrodynamic pressure, and in the energy equation, P_o as the thermodynamic pressure, which is considered spatially uniform. Here, because of the low Mach approximation, the viscous heating $\tau_{ij} \frac{\partial u_i}{\partial x_j}$ and the pressure term $u_i \frac{\partial p}{\partial x_i}$ are neglected. The enthalpy used for non-reacting flows is the sensible enthalpy

$$dh = c_p dT \quad (4)$$

The thermodynamic pressure, temperature and density are coupled through the equation of state

$$P_o = \rho R_g T \quad (5)$$

It should be noted that the scalars' transport equations are formulated in non-conservative form. The need for it will be clearly shown when the temporal integration algorithm is presented. Thermo-physical properties of the fluid are a function of temperature and thermodynamic pressure, where it applies.

2.1. Chemically reacting flows

When a chemically reacting flow is considered, the distribution of the different species constituting the flow must also be tracked. Only $N - 1$ additional equations are then introduced, because the sum of the N equations results in the continuity equation, Eq. (1). The transport equation of the k th species mass fraction Y_k in non-conservative form, using Hirschfelder and Curtiss approximation [33] is

$$\rho \frac{\partial Y_k}{\partial t} = -\rho u_j \frac{\partial Y_k}{\partial x_j} + \frac{\partial}{\partial x_j} \left(\rho D_k \frac{\partial Y_k}{\partial x_j} \right) + \frac{\partial}{\partial x_j} \left(\rho Y_k \left(\frac{D_k}{M_w} \frac{\partial M_w}{\partial x_j} - V_j^c \right) \right) + \dot{w}_k, \quad (6)$$

where $V_j^c = \sum_k (D_k / M_w) (\partial (M_w Y_k) / \partial x_i)$ is a correction velocity to ensure global mass conservation. The term \dot{w}_k represents the chemical reaction rate, D_k is a species mass diffusivity and M_w is the mixture molar mass. The energy equation is solved in its enthalpy form, as shown in Eq. (3). For chemically reacting cases, the enthalpy is equal to the sum of the enthalpy of formation plus the sensible enthalpy, resulting in

$$h = \sum_{k=1}^N Y_k h_k = \sum_{k=1}^N Y_k \left(\Delta h_{f,k}^o + \int_{T_0}^T c_{p,k} dT \right). \quad (7)$$

The heat transfer flux for reacting cases becomes $\dot{q}_j = -\kappa \frac{\partial T}{\partial x_j} - \sum_{k=1}^N \rho h_k ((D_k/M_w)(\partial(M_w Y_k)/\partial x_j) - Y_k V_j^c)$, where the second term on the right-hand side (r.h.s.) represents the transport of energy because of mass diffusion. For the present study, both Soret and Duffour effects are considered to be negligible; thus, the energy equation remains unchanged as defined in Eq. (3).

2.2. Thermodynamic pressure

In low Mach flows, the state Eq. (5) couples the temperature and the density through a spatially uniform thermodynamic pressure. Then, the energy equation acts as a constraint on the flow. Using the transport equations Eqs. (1), (3) and (6) and the state Eq. (5), the velocity divergence constraint for perfect gases becomes

$$\begin{aligned} \frac{\partial u_j}{\partial x_j} = \frac{R_g}{c_p P_o} & \left[\frac{\partial}{\partial x_j} \left(\kappa \frac{\partial T}{\partial x_j} \right) - \left(\frac{c_p}{R_g} - 1 \right) \frac{dP_o}{dt} - \sum_{k=1}^N h_k \dot{w}_k \right. \\ & \left. + \sum_{k=1}^N \rho c_{p,k} \left(\frac{D_k}{M_w} \frac{\partial(M_w Y_k)}{\partial x_j} - Y_k V_j^c \right) \frac{\partial T}{\partial x_j} \right] \end{aligned} \quad (8)$$

Integrating over the computational domain gives an equation for the thermodynamic pressure variation

$$\begin{aligned} \frac{dP_o}{dt} = \frac{1}{\int_V (\frac{c_p}{R_g} - 1) dV} & \left[\int_V \frac{\partial}{\partial x_j} \left(\kappa \frac{\partial T}{\partial x_j} \right) dV - \frac{P_o}{R_g} \int_V c_p \frac{\partial u_j}{\partial x_j} dV - \int_V \sum_{k=1}^N h_k \dot{w}_k dV \right. \\ & \left. + \int_V \sum_{k=1}^N \rho c_{p,k} \left(\frac{D_k}{M_w} \frac{\partial(M_w Y_k)}{\partial x_j} - Y_k V_j^c \right) \frac{\partial T}{\partial x_j} dV \right] \end{aligned} \quad (9)$$

If the system is considered open, this thermodynamic pressure is deemed constant and set to ambient pressure or the reference pressure for the specific case. If the system is closed, a mass conservation is invoked, and the pressure at a given time can be obtained through the total mass in the enclosure and the temperature field

$$M_o = \frac{P_o}{R_g} \int_V \frac{1}{T_{t=0}} dV \quad (10)$$

$$P_o(t) = \frac{M_o R_g}{\int_V \frac{1}{T(t)} dV} \quad (11)$$

3. PRESSURE-VELOCITY COUPLING – FRACTIONAL STEP METHOD

In subsonic flows, such as in the low Mach limit, the Navier–Stokes equations are elliptic. The pressure couples the whole spatial domain and consequently through the momentum equation pressure and velocity are coupled.

In order to solve the pressure-velocity coupling that appears in the momentum equations, Eq. (2), a projection method is used, namely, the fractional step method [12]. It begins by taking the momentum equation, approximating the temporal derivative and introducing a pseudo-velocity \hat{u}_i^l , thus splitting the original equation into two parts

$$\frac{\rho^l \hat{u}_i^l - \rho^n u_i^n}{\Delta t} = \alpha^n \left\{ -\frac{\partial \rho u_j u_i}{\partial x_j} + \frac{\partial \tau_{ij}}{\partial x_j} + \rho g_i \right\}^n \quad (12)$$

$$\frac{\rho^l u_i^l - \rho^l \hat{u}_i^l}{\Delta t} = -\frac{\partial p^l}{\partial x_i} \quad (13)$$

where l and n indicate the current substep and previous time step, respectively. The r.h.s. of Eq. (12) is a function of the temporal integration scheme, denoted by α^n . A multi-step temporal algorithm is used, which is described afterwards in Section 5. In the temporal algorithm prior to computing the momentum equations, the scalars transport equations are solved and the density ρ^l is computed using Eq. (5). The next step of this projection method is to take the divergence of Eq. (13), which results in a Poisson equation

$$\frac{1}{\Delta t} \left(\frac{\partial}{\partial x_i} (\rho^l u_i^l) - \frac{\partial}{\partial x_i} (\rho^l \hat{u}_i^l) \right) = - \frac{\partial}{\partial x_i} \left(\frac{\partial p^l}{\partial x_i} \right) \quad (14)$$

This procedure, denoted as mass projection, results in a constant coefficient Poisson equation. In both predictor and corrector substeps, the pressure Poisson equation is solved using a direct Schur decomposition [34, 35]. Other variants for the fractional step method applied to low Mach flows consider a velocity projection, which results in a variable coefficient Poisson equation [13, 14]. In the constant coefficient Poisson equation, mass divergence at the next time step $(\nabla \cdot (\rho u))^l$ is unknown, but it can be approximated using the mass conservation equation Eq. (1). The temporal derivative of the density is then introduced into Eq. (14). This term has been reported to introduce numerical instabilities [13–15], and no closed form to approximate this time derivative has been reported to be best suited. In this work, the second-order backward approximation to the first derivative at the l substep proposed by Nicoud [13] is used

$$\left. \frac{\partial \rho}{\partial t} \right|^l = \frac{((\Delta t^n + \Delta t^{n-1})^2 - (\Delta t^n)^2) \rho^l - (\Delta t^n + \Delta t^{n-1})^2 \rho^n + (\Delta t^n)^2 \rho^{n-1}}{\Delta t^n \Delta t^{n-1} (\Delta t^n + \Delta t^{n-1})} \quad (15)$$

By using the continuity equation to approximate the mass divergence $\nabla \cdot (\rho u)^l$, mass conservation is enforced. The gas state law Eq. (5) is used in its form at each substep to compute the density. However, energy conservation is not satisfied as it can be seen by the use of the non-conservative form of the energy equation, Eq. (3). As reported by Knikker [14], all three constraints, mass conservation, ideal gas law and energy conservation, can only be met when an iterative time scheme is used. However, the consequence is a higher computational effort per iteration.

4. UNSTRUCTURED DISCRETISATION

The discrete set of equations is obtained employing the finite-volume technique, where the governing equations Eqs. (1)–(3) and (6) in differential form are integrated giving a set of conservation equations to be solved at each control volume (CV).

The generic transport equation in integral form after applying Gauss theorem is

$$\begin{aligned} \int_V \frac{\partial \rho \phi}{\partial t} dV &= - \int_A \rho u_j n_j \phi dA + \int_A \Gamma \frac{\partial \phi}{\partial x_j} \Big|_f n_j dA + \int_V S dV \\ &= -C_c + D_c + S \cdot V, \end{aligned} \quad (16)$$

where ϕ represents any dependent variable (u_i , Y_k and T) and C , D and S represent the convective, diffusive and extra terms, respectively. Approximating the surface integrals as summation over cell faces, the discrete cell-centred convective and diffusive terms become

$$C_c = \sum_f \phi_f \rho_f u_{i,f} n_{i,f} A_f \quad (17a)$$

$$D_c = \sum_f \Gamma_f (\phi_{nbcv} - \phi_{cv}) \frac{A_f}{\delta_f}, \quad (17b)$$

where ϕ_f represents an interpolation of ϕ at a cell face. The details of these interpolations will be discussed later. In the diffusive term, the derivative of the variable at the face is discretised by means

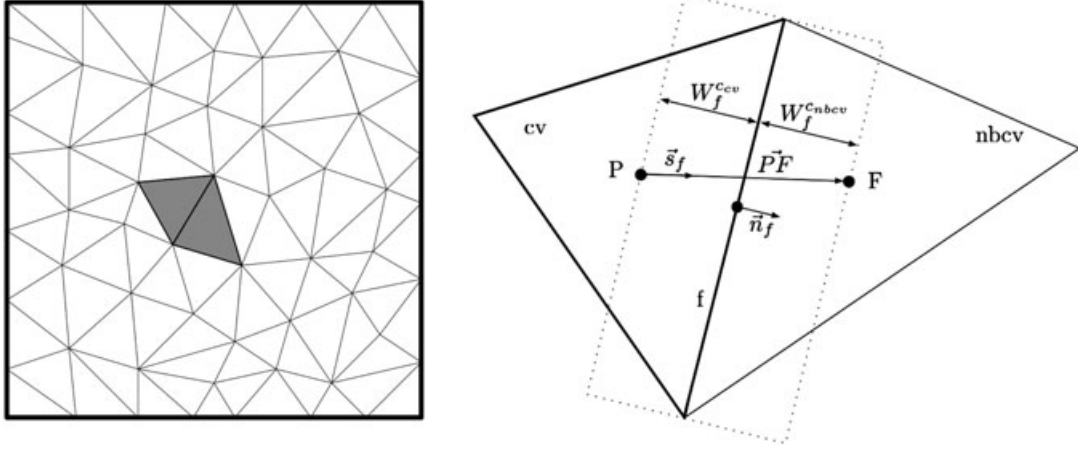


Figure 1. Unstructured mesh (left) and geometrical parameters (right) used to define both collocated and staggered formulations. Points P and F represent the cell centroids for collocated schemes and the cell circumcentres for staggered schemes.

of a two point-centred approximation to the first-derivative central differencing scheme (CDS). The distance δ_f for unstructured meshes is the distance between two nodes projected in the normal direction to the face, $\delta_f = (s_{i,f} n_{i,f})$, where $s_{i,f}$ is the vector from the centroid of the CV to the centroid of the neighbour CV, as it can be seen in Figure 1.

Regarding the scalars, the non-conservative form of the convective term requires the evaluation of the gradient of the scalar. However, using the chain rule, the non-conservative convective can be rewritten as a function of the convective term in conservative form

$$\rho u_i \frac{\partial \phi}{\partial x_i} = \frac{\partial \rho u_i \phi}{\partial x_i} - \phi \frac{\partial \rho u_i}{\partial x_i}, \quad (18)$$

where the first term on the r.h.s. is computed as in Eq. (17a), and the second term is evaluated as the product of the scalar value at cell nodes times the divergence of ρu_i at cell nodes. The latter is evaluated using a least-squares procedure [36].

Having defined the discrete form of the transport equations, in the following, focus is placed on the spatial discretisation of the momentum equations in order to tackle the pressure-velocity coupling. Two formulations for unstructured meshes are here described, namely, the collocated formulation detailed by Trias *et al.* [28] and Jofre *et al.* [29] and the staggered one of Perot [26]. Concerning the scalars, only the collocated one is employed.

The main difference between collocated and staggered formulations is the location of the primary solution variables. Both collocated and staggered schemes place scalar variables (ρ , p , h , T , Y_k) at cell centres and the mass flow is placed at the cell faces. The velocity u_i is stored at the cell centres in the collocated scheme. In the staggered scheme, the mass flux ρu is stored at the face centres.

Collocated formulations are known to suffer from an odd–even decoupling of the pressure field because of pressure and velocity being placed at the same points, as shown by Patankar [37]. Additionally, it has also been shown that collocated formulations do not fully preserve kinetic energy. Morinishi *et al.* [38] showed that the error is of $\mathcal{O}(\Delta t^\alpha \Delta x_i^2)$, with α depending on the temporal integration scheme. However, when dealing with complex geometries or when non-Cartesian grids are considered, the collocated mesh scheme is usually preferred because of its simplicity, as opposed to staggered formulations, which require defining displaced meshes. Construction of these displaced meshes is trivially performed for Cartesian grids, but it is a more complex task for non-Cartesian ones. Nonetheless, the method described by Perot [26] allows these displaced meshes to be built

almost effortlessly. Staggered formulations present the advantage of not suffering from the pressure odd–even decoupling.

4.1. Collocated discretisation

As described by Felten and Lund [25], collocated formulations suffer from two types of error. The first type is related to mass conservation, which also influences kinetic energy conservation. The rationale is that the pressure field obtained from the Poisson equation Eq. (14) ensures mass conserving fluxes at the faces, but not for the primary solution variables, which are located at the cell centres. This results in a pressure-velocity decoupling. In order to avoid it, a pressure correction to the cell-centred velocities is applied. Therefore, once the pressure equation Eq. (14) has been solved, the cell-centred velocities must be corrected using Eq. (13), resulting in

$$u_{i,c}^l = \hat{u}_{i,c}^l - \frac{\Delta t}{\rho_c^l} \left. \frac{\partial p}{\partial x_i} \right|_c, \quad (19)$$

where the cell-centred pressure gradient is evaluated using the Gauss theorem.

The second type of error is related to the reconstruction of the mass flow at the cells' faces. On the predictor stage of the fractional step method[‡], once the pseudo-velocities \hat{u}_i^l have been computed using Eq. (12), the pseudo-mass flow has to be evaluated

$$\hat{m}^l = (\rho \hat{u}_i)_f^l n_{i f} A_f, \quad (20)$$

where $(\rho \hat{u}_i)_f^l$ must be approximated. As shown by Felten and Lund [25], the reconstruction of the variables at the faces is a critical issue. Therefore, in order to minimise errors in the conservation of the kinetic energy, the interpolation at the faces is performed by taking the average between neighbouring cells

$$\rho \hat{u}_i|_f^l = \frac{1}{2} \left(\rho \hat{u}_i|_{cv}^l + \rho \hat{u}_i|_{nbcv}^l \right), \quad (21)$$

where for low Mach flows, the faces mass flux is the average of cell-centred mass fluxes, instead of using the average of cell velocities used by Felten and Lund [25]. Once the velocity at cell centres is known, the mass flow at the cell faces' is reconstructed accordingly

$$\dot{m}^l = (\rho \hat{u}_i)_f^l n_{i f} A_f - \Delta t \left. \frac{\partial p}{\partial x_i} \right|_f^l, \quad (22)$$

where the face pressure gradient is approximated by a centred finite difference $\left. \frac{\partial p}{\partial x_i} \right|_f^l = \frac{(p_{nbcv}^l - p_{cv}^l)}{\delta_f} A_f$ and the pseudo-velocity at the cell faces is obtained through Eqs. (19) and (21)

$$\rho \hat{u}_i|_f^l = \frac{1}{2} \left(\left(\rho u_i|_{cv}^l + \Delta t \left. \frac{\partial p}{\partial x_i} \right|_{cv}^l \right) + \left(\rho u_i|_{nbcv}^l + \Delta t \left. \frac{\partial p}{\partial x_i} \right|_{nbcv}^l \right) \right). \quad (23)$$

The earlier equation is derived imposing mass conservation to the velocity field at the faces. As shown by Jofre *et al.* [29], by taking the divergence of Eq. (13), approximating the volume integrals by summation over the faces and requiring mass conservation at an infinitesimal CV at each face, Eq. (23) is obtained. This aspect is essential to ensure a correct mass conservation. The correction here presented reminds to the one presented by Rhie and Chow [39] based on a momentum-weighted interpolation strategy. Regarding the order of the error in kinetic energy conservation, this scheme gives an error of $\mathcal{O}(\Delta t^2 \Delta x_i^m)$, where $m = \min(2, r)$ and r is the order of the interpolation of the velocities to the face.

[‡]Not to be confused with the predictor substep of the predictor–corrector time integration scheme.

4.2. Staggered discretisation

As stated previously, staggered formulations place velocity and pressure at different grid locations. This methodology presents the advantage that inherently conserves momentum, kinetic energy and circulation. Additionally, it does not present the odd–even decoupling found in collocated schemes. Thus provided that the discrete operators are conservative, this staggered scheme is fully conservative. These advantages come at the cost of requiring the construction of displaced meshes, which in structured meshes are easily built, but on unstructured meshes, it is not a straightforward task.

The method here employed follows the formulation by Perot [26], who proposes a technique to construct a displaced CV at each face and shows that the overlapping of CVs does not represent an issue. The construction of the staggered cells is sketched in Figure 1. The width of the displaced CV is defined as $W_f = W_f^{cv} + W_f^{nbcv}$, where W_f^m is the distance from the face circumcentre to the ‘ m ’ neighbour cell circumcentre (remember that nodes are located at the cell centroid). The volume of the displaced CV is then $V_f = W_f A_f$. Subindexes ‘ cv ’ and ‘ $nbcv$ ’, which refer to cells sharing the same face, are here maintained for consistency with the collocated formulation. The described method assumes that cells have a circumcentre, which is not required to be within a cell. However, highly distorted grids can impact the accuracy of the method.

The staggered formulation uses the displaced mesh to integrate the face normal mass fluxes, ρu . Therefore, integrating Eq. (12) over each displaced cell and taking the dot product with the face normal vector, the staggered form of the fractional step is obtained, where the primary solution variable is the face normal mass flux

$$\frac{(\rho \hat{u})_f^l - (\rho u)_f^n}{\Delta t} V_f = \alpha^n \{-C_{i,f} n_{i,f} + D_{i,f} n_{i,f} + \rho_f g_i n_{i,f}\}^n, \quad (24)$$

where convective and diffusive terms have to be calculated at the faces. Notice that the integrated variable is a scalar value located at the face and in the face normal direction. In the present formulation, convective and diffusive terms are interpolated to the faces from the cell-centred values using a weighted sum

$$C_{i,f} = W_f^{cv} \frac{C_{i,cv}}{V_{cv}} + W_f^{nbcv} \frac{C_{i,nbcv}}{V_{nbcv}} \quad (25a)$$

$$D_{i,f} = W_f^{cv} \frac{D_{i,cv}}{V_{cv}} + W_f^{nbcv} \frac{D_{i,nbcv}}{V_{nbcv}}, \quad (25b)$$

where $C_{i,cv}$ and $D_{i,cv}$ are calculated using Eq. (17). Analogously, for the pressure correction Eq. (13)

$$(\rho u)|_f^l = (\rho \hat{u})|_f^l - \Delta t \left(p_{nbcv}^l - p_{cv}^l \right) \frac{A_f}{V_f}, \quad (26)$$

where, because of the method of construction of the displaced cells around the cells’ faces, the pressure gradient is computed as the pressure difference between the displaced CV faces. Thereafter, the procedure is akin to the one presented for the collocated scheme. Taking the divergence of Eq. (26), a Poisson equation, Eq. (35), is obtained, where again the mass divergence at the next step is approximated through the continuity equation by the temporal derivative of the density Eq. (15). Once it has been solved, the face mass fluxes are corrected by means of Eq. (26) without any further modifications.

Lastly, one critical aspect remains to be considered for Perot’s staggered formulation. The convective and diffusive operators have been approximated at the cell faces using their corresponding values at the cell centres. However, in order to compute these values at the cell centres, the velocity field at those locations must be computed. In this regard, two approaches are used in this work, the first-order reconstruction (STAGG1) proposed by Perot [26] and a polynomial reconstruction method (STAGG2) proposed by Jofre *et al.* [29].

Perot's first-order reconstruction applies Gauss' divergence theorem to the product of the velocities and the position r_i at each cell. However, in low Mach flows, the mass flux $\rho u_{i,c}$ is used for the first-order reconstruction instead

$$\int_{V_c} \rho_c u_{i,c} |^l dV + \int_{V_c} r_i \frac{\partial \rho_c u_{j,c} |^l}{\partial x_j} dV = \sum_f \int_{A_f} (r_i (\rho u_j |^l)) \cdot n_j dA, \quad (27)$$

where $r_i = x_i - x_{0,i}$ represents the position with respect to the cell circumcentre. Then, assuming a constant mass field within the cell, thus making a first-order approximation within the cell and rendering the second term on the left-hand side (l.h.s.) equal to zero, the cell-centred velocity is computed through

$$u_{i,c}^l = \frac{1}{\rho_c^l V_c} \sum_f r_{i,f}^c \rho_f u_{j,f}^l n_j A_f, \quad (28)$$

where $r_{i,f}^c = x_{i,f}^{fg} - x_{i,c}^{cc}$ is the vector from the cell circumcentre $x_{i,c}^{cc}$ to the face centroid $x_{i,f}^{fg}$.

The second reconstruction method (STAGG2) uses a least square procedure to obtain the cell-centred velocities from the faces' mass fluxes, which is an extension of the method proposed by Jofre *et al.* [29], where they used the velocities for the reconstruction. To that end, the cell-centred velocity is approximated by a polynomial function around the cell centroid ($u_c(r) = \mathbf{a} + \mathbf{b}x + \mathbf{c}y + \mathbf{d}z$) with the restriction that at the cell faces the computed mass fluxes have to be recoveredp

$$\rho_c u_{i,c}(r) n_{i,f} = (\rho u) |_f. \quad (29)$$

Hence, a linear system of equations is obtained where the coefficients (\mathbf{a} , \mathbf{b} , \mathbf{c} and \mathbf{d}) of the polynomial are the unknowns. The resulting system is overdetermined, because of the higher number of faces than unknowns. Therefore, a least-squares method is used to solve the system. As it can readily be seen, this second approach is computationally more expensive than the STAGG1 method, mainly due to the need of solving a system of equations for each cell.

4.3. Face interpolation schemes

As previously stated, when the convective and diffusive operators were discretised, there remained to be detailed the interpolations of the face-centred values for the convective term. The diffusive term, as described previously in Eq. (17), is discretised using a CDS.

4.3.1. Momentum convective. As shown by Verstappen and Veldman [27], in order to ensure good stability properties of the numerical algorithm, even at high Reynolds numbers with coarse meshes, it is necessary to preserve the properties of the differential operators in their discrete counterparts. Therefore, the discrete convective operator is required to be skew symmetric, the negative conjugate transpose of the discrete gradient operator to be exactly equal to the mass divergence operator and the diffusive terms to be strictly dissipative, being the diffusive operator symmetric and positive definite. These requirements are mainly placed for the momentum equations, from which kinetic energy conservation is derived. Therefore, in the momentum equations, cell face values required by the convective operator are interpolated using a second-order SP interpolation, which produces a skew symmetric discretisation

$$\phi_f = \frac{1}{2}(\phi_{cv} + \phi_{nbcv}). \quad (30)$$

This formulation applied to incompressible flows has been shown to preserve kinetic energy in the inviscid limit [27–29]. Low Mach flows in the inviscid limit ($\mu \rightarrow 0, \kappa \rightarrow 0$) reduce to the incompressible case, as can be deduced from Eq. (8). Hence, the same conservation properties of this scheme reported for incompressible flows also apply for low Mach flows. Kinetic energy preservation is an important issue of the proposed methodology, which enables performing stable simulation on any grid, as described by Verstappen and Veldman[27]. Still, this applies to the momentum equations. Further considerations are required for the scalar equations.

Regarding the diffusive operator, the use of the CDS results in a symmetric and positive definite matrix.

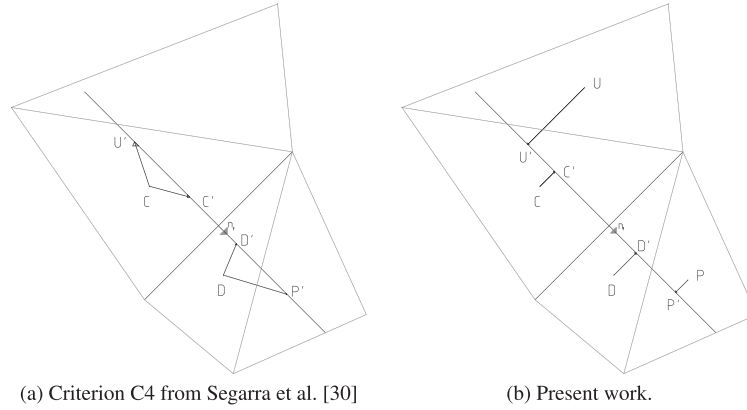


Figure 2. Points for the quadratic upstream interpolation for convective kinematics (QUICK) scheme interpolations.

4.3.2. Scalars convective. Concerning the transport equations for scalars, such as enthalpy, temperature or mass fractions, the earlier requirements of kinetic energy preservation do not apply. Hence, for the scalar equations, instead of using the SP scheme, a second-order CDS (CDS2) with unequal weights suitable for non-uniform meshes is adopted

$$\phi_f = \phi_D \left(\frac{x_f - x_C}{x_D - x_C} \right) - \phi_C \left(\frac{x_f - x_D}{x_D - x_C} \right), \quad (31)$$

where C and D denote the neighbouring cell nodes, as depicted in Figure 2.

Still, additional considerations have to be taken into account. When the local Peclet is high, centred approximations to the derivatives were found to introduce oscillatory modes in the problem resolution [37]. Therefore, upwinding-like interpolations were proposed to address this stability issue. The classical upwind difference scheme (UDS), where the face value is approximated by the upwinding cell value, is known to be dissipative and to introduce ‘false diffusion’ effects, which are not desired in the current framework. Higher-order upwinding interpolations such as the quadratic upstream interpolation for convective kinematics (QUICK) [40] are able to deal with ‘false diffusion’ effects, while reducing their dissipative effect. As opposed to Cartesian meshes, where the upwind and downwind nodes can readily be selected, when dealing with unstructured meshes, several options are feasible as described by Segarra *et al.* [30]. In this work, an extension to criterion C4 is used.

Criterion C4 generated new points on the face normal direction using only the nodal values and the gradient of the CVs to which the face belonged, denoted in Figure 2(a) as points C and D . In this work, instead of generating two points from the same nodal point, each point is the projection of a neighbouring CV node on the face normal direction, as shown in Figure 2(b). Then, the projected variables’ values are obtained using their nodal value and the gradient at their CV. The advantage of the present method is that in case of using a Cartesian mesh, because the nodal points would already be on the face normal direction, the projected points would be the CV nodes, thus recovering the original QUICK scheme. On the other hand using, Criterion C4 two new points would still be generated from the same source point; therefore, the final approximation would be of lower order.

Having defined the upwind and downwind nodes, face values using the QUICK scheme [40], with Figure 2(b) notation and considering non-equidistant placement of the projected nodes, are computed as

$$\bar{x} = \frac{x - x_{U'}}{x_{D'} - x_{U'}} \quad (32a)$$

$$\bar{\phi} = \frac{\phi - \phi_{U'}}{\phi_{D'} - \phi_{U'}} \quad (32b)$$

$$\bar{\phi}_f = \bar{x}_f + \frac{\bar{x}_f(\bar{x}_f - 1)}{\bar{x}_{C'}(\bar{x}_{C'} - 1)}(\bar{\phi}_{C'} - \bar{x}_{C'}), \quad (32c)$$

where the overbar denotes non-dimensional values, and values in the normal face direction are obtained using the cell-centred gradient

$$\phi_{C'} = \phi_C + \nabla\phi|_C \cdot \mathbf{CC}' \quad \phi_{D'} = \phi_D + \nabla\phi|_D \cdot \mathbf{DD}' \quad \phi_{U'} = \phi_U + \nabla\phi|_U \cdot \mathbf{UU}'.$$

For the QUICK scheme on unstructured meshes, this first interpolation or projection diminishes its accuracy, and consequently, its high-order properties can be lost. This aspect is discussed in Section 6.1. Nonetheless, false diffusion effects are greatly diminished. In the analysis, CDS2, UDS and QUICK interpolation schemes are used for the scalars' convective term.

4.4. Boundaries

Regarding values at boundaries of the computational domain, both collocated and staggered formulations deal with them similarly. Dirichlet-type conditions are imposed at face nodes. Neumann-type conditions are applied analogously to the diffusive flux. Therefore, the flux at the face is computed using a one legged two point approximation to the first derivative. Concerning the displaced meshes in the staggered formulation, no displaced CVs are created on the boundary faces. Similarly, in the evaluation of the convective operator, because values at the boundary faces are known, no interpolations such as Eq. (30) are needed.

5. TEMPORAL INTEGRATION ALGORITHM

In this section, the explicit two-step temporal integration algorithm is described. Predictor–corrector schemes were proposed for low Mach number flows because of numerical instabilities observed when a fully one step explicit time integration scheme was used [11].

A variant of the predictor–corrector scheme shown by Najm *et al.* [11] is proposed here to solve the set of equations Eqs. (1)–(3) and (5). When chemically reacting flows are considered, Eq. (6) is also taken into account. The significant difference with respect to the aforementioned temporal scheme is that in this work, the density is computed through the gas state law and scalars are transported, namely, enthalpy and species mass fractions. Similarities may also be found between the present algorithm and the *algorithm A1* of Knikker [14], which solves the energy equation in temperature form and uses a semi-implicit third-order Runge–Kutta/Crank–Nicolson scheme, and the predictor–corrector scheme used by Lessani and Papalexandris [15], which also solves the energy equation in temperature form. In both cases, assumptions regarding constant properties are made. Regarding the energy equation, in the current approach, the transport of the enthalpy results in a transport equation of a conserved scalar, in the absence of radiation heat losses.

The pressure-velocity coupling is solved using a fractional step projection method as described Section 3. This fractional stepping is discretised using both collocated [25] and staggered [26] formulations. In the predictor step, a second-order Adams–Bashforth time integration scheme is used to calculate the intermediate scalar and velocity fields. A pressure correction step ensures that the continuity equation, Eq. (1), is satisfied. The corrector step uses a Crank–Nicolson time integration scheme to advance the scalar fields. The velocity is reintegrated using again an Adams–Bashforth scheme, with the density at the next time step ($n + 1$). This corrector step also involves the resolution of a Poisson equation.

In explicit temporal algorithms, as shown by Knikker [14], the scalar transport equations must be expressed in non-conservative form because the density is computed afterwards, being itself a function of the previously computed scalars. Unless an implicit approach is taken, energy conservation Eq. (3), gas state law Eq. (5) and mass conservation Eq. (1) cannot be satisfied simultaneously.

The predictor–corrector algorithm is the following

5.1. Predictor – First step ($l = 1$)

1. Scalars are advanced using an Adams–Bashforth scheme

$$\rho^n \frac{\phi^l - \phi^n}{\Delta t} = \frac{3}{2} \left(\rho^n \frac{\partial \phi}{\partial t} \Big| ^n \right) - \frac{1}{2} \rho^{n-1} \frac{\partial \phi}{\partial t} \Big|^{n-1}, \quad (33)$$

where $\phi = Y_k$ for the species equation and $\phi = h$ for the energy equation. In Eq. (33), the first and second terms on the r.h.s. are evaluated using Eq. (6) for the species and Eq. (3) for the energy transport, at time steps n and $n - 1$. In these scalar transport equations, no distinction is made between collocated and staggered schemes as in both formulations scalar variables are stored at cell centres.

2. Evaluate the thermodynamic pressure P_o from Eq. (11), if it is not constant.
3. Evaluate the density ρ^l from the state equation Eq. (5), using the predictor temperature T^l .
4. Pressure corrector step.

- (a) Calculate the pseudo velocities using Eq. (12)

$$\frac{\rho^l \hat{u}_i^l - \rho^n u_i^n}{\Delta t} = \frac{3}{2} \left(\frac{\partial \rho u_i}{\partial t} \Big| ^n \right) - \frac{1}{2} \frac{\partial \rho u_i}{\partial t} \Big|^{n-1} \quad (34)$$

When using the collocated formulation, the temporal derivatives of the cell-centred velocity in the earlier equation are computed using Eq. (12). When dealing with the staggered formulation, mass fluxes at the cell faces are integrated in time and computed through Eq. (24).

- (b) Solve the Poisson equation.

$$\frac{\partial}{\partial x_i} \left(\frac{\partial p^l}{\partial x_i} \right) = \frac{1}{\Delta t} \left[\frac{\partial}{\partial x_i} (\rho^l \hat{u}_i^l) - \frac{\partial}{\partial x_i} (\rho^l u_i^l) \right], \quad (35)$$

where the pseudo-mass flow, first term on the r.h.s., is obtained from Eq. (20) in the collocated scheme. This pseudo-mass flow is directly obtained from the time integration, Eqs. (24) and (34) in staggered meshes. Mass divergence at the next substep is approximated using the continuity Eq. (1)

$$\frac{\partial}{\partial x_i} (\rho^l u_i^l) = - \frac{\partial \rho^l}{\partial t} \Big| ^l$$

- (c) Calculate the predictor velocities

$$\frac{\rho^l u_i^l - \rho^l \hat{u}_i^l}{\Delta t} = - \frac{\partial p^l}{\partial x_i}. \quad (36)$$

This correction is applied to cell-centred velocities in collocated schemes, while it is applied to face-centred mass fluxes in staggered schemes.

- (d) Final computations have to be performed for both formulations, as described in the previous section. In short, in the collocated scheme, the faces mass flow have to be computed using Eq. (22). Analogously, in the staggered scheme, the cell-centred velocities have to be reconstructed from the face-centred ones using either STAGG1 or STAGG2 reconstruction method.

5.2. Corrector – Second step ($l = 2$)

For the sake of brevity, comments regarding staggered and collocated differences have been omitted in this subsection. The reader is referred to Section 5.1 for differences between both spatial formulations within the temporal algorithm.

1. With the values computed at the Predictor step, the r.h.s. of Eq. (3) is used to evaluate the time derivative of the predictor enthalpy $\left(\rho^{l-1} \frac{\partial h}{\partial t} \Big|^{l-1}\right)$ and the r.h.s. of Eq. (6) to evaluate the time derivative of the predictor mass fraction $\left(\rho^{l-1} \frac{\partial Y_k}{\partial t} \Big|^{l-1}\right)$. Then, the time derivative at the next time is evaluated using a Crank–Nicholson scheme

$$\rho^{l-1} \frac{\phi^{n+1} - \phi^n}{\Delta t} = \frac{1}{2} \left(\rho^n \frac{\partial \phi}{\partial t} \Big|^n + \rho^{l-1} \frac{\partial \phi}{\partial t} \Big|^{l-1} \right), \quad (37)$$

where $\phi = Y_k$ for the species equation and $\phi = h$ for the energy equation.

2. Evaluate the thermodynamic pressure P_o from Eq. (11), if it is not constant.
3. Using the ideal gas law Eq. (5), the density field at the next time step is computed.
4. Finally, the pressure corrector step is used to compute the velocity field.
 - (a) Calculate the pseudo velocities using Eq. (12)

$$\frac{\rho^{n+1} \hat{u}_i^l - \rho^n u_i^n}{\Delta t} = r.h.s. \{ Eq. (34) \} \quad (38)$$

- (b) Solve the Poisson equation

$$\frac{\partial}{\partial x_i} \left(\frac{\partial p^{n+1}}{\partial x_i} \right) = \frac{1}{\Delta t} \left[\frac{\partial}{\partial x_i} (\rho^{n+1} \hat{u}_i^l) - \frac{\partial}{\partial x_i} (\rho^{n+1} u_i^{n+1}) \right], \quad (39)$$

where, as done in the predictor stage, the momentum divergence $\nabla \cdot (\rho^{n+1} u^{n+1})$ is replaced, using the continuity Eq. (1), by the density time derivative Eq. (15).

- (c) Calculate the velocities at the next time step

$$\frac{\rho^{n+1} u_i^{n+1} - \rho^{n+1} \hat{u}_i^l}{\Delta t} = - \frac{\partial p^{n+1}}{\partial x_i}. \quad (40)$$

- (d) In collocated schemes, the face mass flow \dot{m}_f^{n+1} has to be computed using Eq. (22). Analogously, in staggered schemes, the cell-centred velocities $u_{i,c}^{n+1}$ have to be reconstructed from the face-centred mass fluxes using either STAGG1 or STAGG2 reconstruction method.

6. NUMERICAL TESTS

In the following, the numerical schemes presented are tested in order to study the effect of non-structured meshes. Specifically, unstructured triangular meshes are employed. In general, uniform meshes have been used in order to facilitate the comparison between computations. In unstructured meshes, different parameters may affect the accuracy of the schemes, that is, skewness or orthogonality. Still, common practice in computational fluid dynamics is to seek for meshes with smooth changes of geometrical properties. Hence, the results here shown are indicative of the effect of switching from structured to unstructured meshes. The general purpose unstructured and parallel object-oriented CFD code *TermoFluids* [41] is used in this work. Three test cases are discussed. *Test case 1* consists in a numerical reconstruction of a solenoidal field, which is used to assess the accuracy of the interpolation schemes. *Test case 2* is a differentially heated cavity under a large temperature difference, through which the spatial discretisation of the low Mach equations is analysed. *Test case 3* is a self-igniting turbulent jet flame, whereby the effect of the spatial discretisations on the transient algorithm is evaluated. This last case serves also to ascertain the behaviour of the algorithm to handle turbulent flows.

6.1. Test case 1 – Interpolation schemes accuracy

6.1.1. *Case definition.* The accuracy of the presented interpolation schemes is studied by means of an exact sinusoidal function, *test case 1*. The reduction of the interpolations numerical error with respect to the exact analytical value provides the order of accuracy. The target function to be interpolated is a sinusoidal function

$$= \frac{1}{2\pi L} \sin(2\pi Lx) \cos(2\pi Ly). \quad (41)$$

This function is used twofold, as the function to be interpolated at the faces and as a stream function from which the velocity field is derived by taking the rotational of the function $\vec{u} = \nabla \times \psi$

$$\begin{aligned} u_x &= -\sin(2\pi Lx) \sin(2\pi Ly) \\ u_y &= -\cos(2\pi Lx) \cos(2\pi Ly) \\ u_z &= 0 \end{aligned} \quad (42)$$

This velocity field is used by the upwinding schemes to determine the upwind and downwind nodes. The numerical domain is a cube of length unit ($L = 1$) in each dimension. To carry out the grid refinement study, instead of creating several meshes, the length scale, or wavelength, of the sinusoidal function is modified. With this strategy, a single mesh of n_{CV} volumes is generated and then the mesh is coarsened by increasing the length scales of the function with respect to the mesh average spacing. Therefore, in order to quantify the amount of scales actually being captured by the mesh, two quantities have to be defined. In the first place, the average mesh volume is defined as $V_{avg} = \frac{1}{n_{CV}} \sum_c V_c$, which allows defining an average mesh spacing as $\Delta x_{avg} = \sqrt[3]{V_{avg}}$. Secondly, the effective length of the domain is defined as $L_{eff} = 1/L$, where L is an integer value, which controls the sinusoidal wavelength. In consequence, the relative mesh size is $\Delta x_{avg}/L_{eff} = \Delta x_{avg} L$.

In order to assess the influence of the unstructured meshing on the face interpolations, two meshes were generated: a structured Cartesian one and a triangular unstructured one (see Figure 1 for the latter mesh). Both meshes have similar average mesh spacings, which ranged from 0 to 0.4. For each relative mesh size, the values of the function Eq. (41) were interpolated at the faces using the analytical values at the cell centres. The 0 relative mesh spacing corresponds to a uniform function ($\psi = 0$). In both structured and unstructured cases, the meshes were uniform, so that all elements had similar geometrical properties. Coarsening and refinement was achieved by changing the function length scale. The motivation of this choice is to easily compare results obtained using structured and unstructured meshes. Still, other geometrical factors, such as skewness, could still be investigated, but are not here considered for the sake of simplicity.

The error ε is then computed as the root mean square between the numerical approximations and the analytical values computed at the faces

$$\varepsilon = \sqrt{\frac{1}{n_F} \sum_f \varepsilon_f^2}, \quad (43)$$

where ε_f is the error in each face value and n_F is the number of faces.

6.1.2. *Face interpolation analysis.* The errors of the interpolations along with their accuracy are plotted in Figure 3. Four interpolation methods are here presented: the SP scheme, which is equivalent to an average, the UDS, the QUICK and, for completion, a CDS using criterion IIa of Segarra *et al.* [30] (CDS2), which makes a linear interpolation between neighbouring nodes and takes into account non-equal distances between the face and the neighbouring nodes.

A first aspect to be highlighted is that the order of accuracy of the different methods is the expected on structured meshes. On unstructured meshes, the order decreases for both the SP and the QUICK schemes. The UDS' order of accuracy remains almost unchanged. However, the cause for the deterioration is different for each scheme. On the one hand, in the QUICK scheme, as described

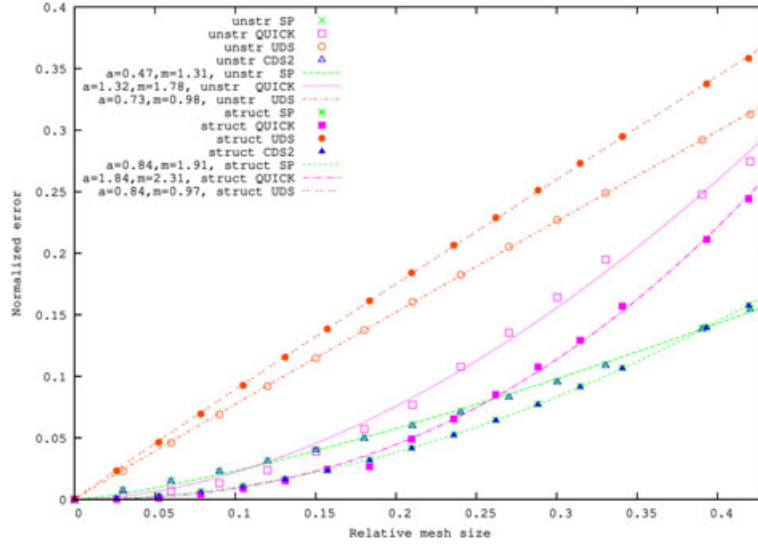


Figure 3. *Test case 1* – Accuracy of the numerical interpolations in structured (struct) and unstructured (unstr) meshes. Dots represent the computed errors, using (43), and lines show the accuracy of each interpolation in the form $\varepsilon = ah^m$, where h denotes the mesh spacing and m indicates the order of accuracy.

previously, the gradients of the cell values are used to approximate the value on the normal direction to the face. This intermediate interpolation is a first-order approximation, which is responsible for the reduction of the interpolation order. On the other hand, central difference schemes, both SP and CDS2, mainly deteriorate because of non-orthogonal effects. Additionally, comparing the SP with the CDS2, both schemes behave almost identically on both structured and unstructured meshes, indicating that the non-equal weights in the CDS are of minor importance in contrast to non-orthogonal effects.

It should be noted that the UDS on unstructured meshes presents lower errors than on structured meshes. This may be attributable to the likely alignment of the unstructured mesh with the solution. Nonetheless, in both cases the accuracy of the scheme is first order as expected.

Considering these results, it can be seen that the slight errors introduced using SP discretisations in the momentum equations, compared with CDS, are compensated by the reported gain in numerical stability [25, 27] when using kinetic energy preserving formulations in turbulent flows. From these results, it can also be inferred that low-order approximations present in the construction of the QUICK on unstructured meshes cause a deterioration of the scheme properties. Nonetheless, the accuracy order of the QUICK scheme is higher than the UDS and even SP scheme.

It should be noted that although the QUICK scheme presents a higher order of accuracy, on coarse meshes, the SP produces a lower level of error. A reason for this behaviour is that the QUICK uses farther located nodes compared with the other schemes, and consequently, in too coarse meshes, the QUICK uses information located too far away, which deteriorates the interpolation. Nonetheless, as the mesh is refined, the errors of the QUICK scheme become lower and at a faster rate than the SP. Therefore, in scalar transport equations, the QUICK scheme is a good alternative in cases where due to stability issues, centred approximations are not viable.

Finally, although effects such as skewness are not presented, it is found that the trend holds. In distorted grids, the properties of the numerical schemes deteriorate.

6.2. Test case 2 – Analysis of the spatial discretisations

6.2.1. *Case definition.* The differentially heated square cavity, *test case 2*, benchmark case [31, 42] of side $L = 1$ under a large temperature difference ($\Delta T = 720$ K) is used. The cavity left wall is at a high temperature (T_h) and the right wall is at a low temperature (T_c). These temperatures are related to the temperature difference by $\epsilon = \frac{T_h - T_c}{2T_0}$. Here, a value of $\epsilon = 0.6$ has been taken, in order to match the benchmark case. The temperature ratio defined between the highest temperature T_h and

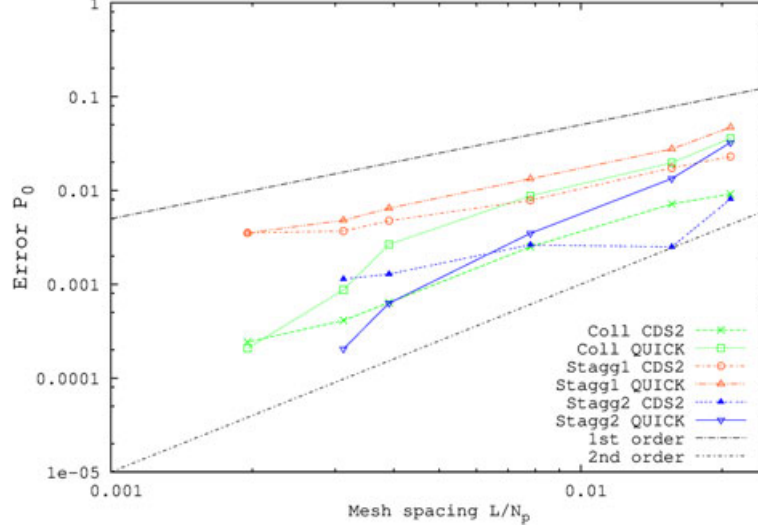


Figure 4. *Test case 2* – Normalised numerical error for the thermodynamic pressure using unstructured meshes. The error is defined as the difference between current results and the benchmark value [42]. For comparison, short-dashed-dotted and long-dashed-dotted lines are plotted, showing first-order and second-order convergence rates. Mesh spacing is expressed in terms of equivalent uniform structured mesh number of points, N_p .

Table I. Results for the differentially heated cavity with $Ra = 10^6$ using a mesh spacing of $1/320$.

Discretisation	Collocated		Staggered (STAGG2)		Reference [42]
Case	Unstructured		Structured	Unstructured	
Scheme	CDS2	QUICK	CDS2	QUICK	—
$P_o/P_{o,0}$	0.9249	0.9237	0.9262	0.9250	0.9245
Nu_h	8.70965	8.6694	8.6742	8.6742	8.6866
Nu_c	8.69889	8.6285	8.6739	8.6358	8.6866
$\frac{Nu_h - Nu_c}{0.5(Nu_h + Nu_c)}$	0.1236%	0.4736%	0.0030%	0.5948%	0%

CDS2, second-order central differencing scheme; QUICK, quadratic upstream interpolation for convective kinematics.

the lowest T_c is 4. As reported by Najm [11], for ratios higher than 2 at least a predictor–corrector scheme, as the one here proposed, is necessary.

The top and bottom walls are considered adiabatic. The fluid filling the cavity is air with a constant Prandtl number ($Pr = 0.71$) and a constant specific heat capacity ($c_p = \gamma R_g / (\gamma - 1)$) where $R_g = 287 \text{ J}/(\text{kg K})$ and $\gamma = 1.4$). Its dynamic viscosity and thermal diffusivity follow Sutherland’s law

$$\frac{\mu(T)}{\mu_{ref}} = \left(\frac{T}{T_{ref}} \right)^{3/2} \frac{T_{ref} + 110.5}{T + 110.5} \quad (44a)$$

$$\kappa(T) = \frac{\mu(T)c_p}{Pr}, \quad (44b)$$

where the reference temperature for this expression has been taken as $T_{ref} = 273 \text{ K}$ and the reference viscosity is $\mu_{ref} = 1.68 \cdot 10^{-5} \text{ kg}/(\text{m s})$. The ideal gas law Eq. (5) is used to calculate the density. The Rayleigh number $\left(Ra = Pr \frac{g \rho_0^2 \Delta T L^3}{T_0 \mu_0^2} \right)$ considered here corresponds to the laminar regime ($Ra = 10^6$). With these parameters and the reference conditions ($P_{o0} = 101325 \text{ Pa}$, $T_0 = 600 \text{ K}$ and $\rho_0 = P_{o0}/(R_g T_0)$), the problem is defined.

To study the accuracy of the described predictor–corrector scheme on non-structured meshes, several uniform triangular unstructured meshes were created (Figure 1), whose mesh spacings were L/N_p , where N_p is the number of points at the boundaries. With this definition of the mesh spacing equivalent structured uniform, or Cartesian, meshes are easily defined[§]. Uniform meshes were chosen in order to minimise variations in mesh properties such as cells’ aspect ratio, measuring the ratio between the smallest cell’s face area and its biggest, and orthogonality factor, measuring the angle between a face normal and the vector joining the neighbours cells centroids.

6.2.2. *Global scheme behaviour.* Figure 4 shows the numerical errors of the thermodynamic pressure P_o , where the error is defined with respect to the reference case [42], shown in Table I. It can be seen that the convergence rate of the global algorithm is between first and second order.

The collocated scheme, using either CDS2 or QUICK in the energy equation, and the staggered scheme using STAGG2 reconstruction method with the QUICK, show similar results, being their convergence rate close to second order. The STAGG2 method with the CDS2 shows first-order accuracy, which indicates that interpolation errors in the energy equation because of the CDS2 affect the cell-centred velocities reconstruction. The staggered scheme using the STAGG1 reconstruction method shows a lower convergence rate, which is of first order. This lower order of convergence for the STAGG1 will be discussed in the following, along with convergence rate of the Nusselt number at the wall. Comparing the curves for the CDS2 and the QUICK scheme, it can be seen that the errors on the coarse meshes are noticeably higher for the QUICK scheme, which is consistent with the results of the first test case (Section 6.1). However, when finer meshes were used, the QUICK scheme delivered errors similar to the CDS2 scheme. As was mentioned in Section 4, momentum equations are solved using SP, while different schemes are used for the scalar transport equations. It can be seen that accurate results are obtained.

Figure 5 shows the error for the Nusselt number at the hot wall with respect to the reference case [42]. The evaluation of the heat fluxes is performed analogously to the evaluation of the diffusive flux in the discrete transport equations, Eq. (17b).

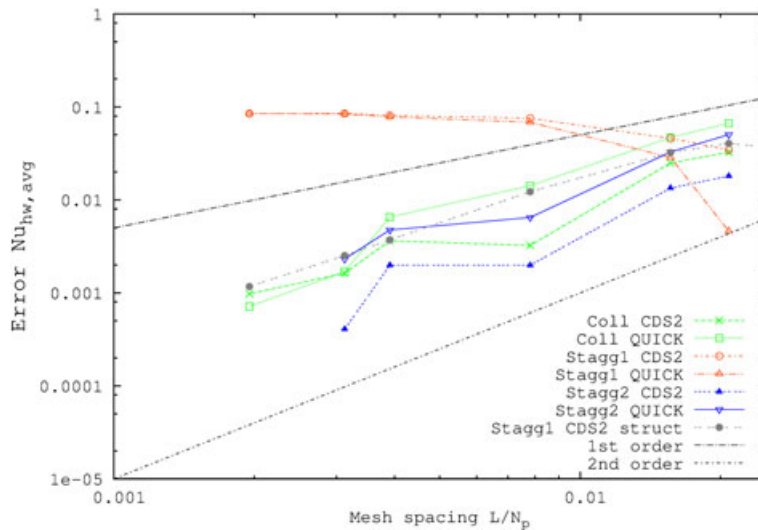


Figure 5. *Test case 2* – Normalised numerical error of the averaged Nusselt number at the hot wall. The error is defined as the difference between current results and the benchmark value [42]. For comparison, short-dashed-dotted and long-dashed-dotted lines are plotted, showing first-order and second-order convergence rates, respectively. Mesh spacing is expressed in terms of equivalent uniform structured mesh number of points, N_p .

[§]For example, if a uniform structured mesh were to be used to discretise, the horizontal direction of the square cavity with $N_p = 64$, the mesh spacing would be $1/64 = 0.0156$

As described for Figure 4, similar trends are observed regarding the order of accuracy for both collocated and structured staggered schemes. The global behaviour of the algorithm is between first and second order, with the exception the staggered scheme using STAGG1 reconstruction method.

First-order accuracy for the local Nusselt number is expected because of the approximation to the first derivative, where a two point one legged stencil is used. However, globally, the Nusselt number is seen to behave between first and second order. The influence of the different schemes, which were used for the convective term, is of minor importance, causing small variations on the actual error.

Considering the first-order accuracy for a local value, such as the Nusselt number at the wall, and the almost second-order accuracy for a global value, such as the thermodynamic pressure and the average Nusselt number at the walls, serves to illustrate the increase in accuracy from local approximations of the operators to the global scheme, because of error cancelling within the mesh [43].

6.2.3. Staggered velocity reconstruction analysis. It must be highlighted that the results obtained with the staggered formulation using the STAGG1 reconstruction method on unstructured meshes show an accuracy of order zero, regardless of the convective discretisation scheme. Further tests using structured Cartesian meshes with the STAGG1 show an accuracy between first and second order. Then, considering that correct results are achieved using the STAGG2 reconstruction method, regardless of the interpolation scheme, and the STAGG1 reconstruction method when applied to quadrangular meshes, it is concluded that the error source is the velocity reconstruction. Analysis of the velocity profiles obtained with the STAGG1 reconstruction method and comparing them with those of the STAGG2 reconstruction and those of the collocated formulation reveal that near the boundary, the velocity peaks are notably lower when the STAGG1 reconstruction is used. Further, in general, the maximum velocities in the domain are also lower when the STAGG1 method is used. Thus, the errors in reconstructing the cell-centred velocities affect the evaluation of the convective term, which in turn affect the magnitude of the diffusive term. Structured meshes do not suffer from this deterioration of the solution because of their inherent geometric properties. Still, it can be seen in Figure 5 that results obtained using the STAGG1 method converge to a solution, indicating that the computed velocity fields on each mesh are intrinsically coherent, although incorrect. Additional simulations were conducted where the second term on the l.h.s. of Eq. (27) was not assumed to be zero, to test the influence of this assumption. However, steady-state results did not vary because at the stationary state, mass divergence is zero, because transient density variations are null. Therefore, higher-order approximations are required for the cell-centred velocities reconstruction, such as the STAGG2 reconstruction method, which is shown to provide accurate results. However, as previously stated, the STAGG2 method is computationally more demanding, which hinders its viability. Results for the finer mesh are not reported for the STAGG2 method because of computational limitations. However, it can be seen that the staggered method using the STAGG2 reconstruction shows a similar trend as the collocated method.

With respect to the cold wall, trends are similar as at the hot wall although minor discrepancies are noticeable. The reason is that the boundary layer is thinner at the cold wall than at the hot wall; therefore, smaller grid spacings are required to correctly characterise the thermal boundary layer at the cold wall. However, in this work, successive uniform meshes have been used.

6.2.4. Conservation properties. In the current formulation, density is evaluated using the ideal gas law Eq. (5). Then, mass conservation is enforced through the Poisson Eq. (14), as in this equation, mass divergence is substituted by the density time derivative. Hence, the Poisson equation enforces mass conservation through the pressure field. Consequently, mass conservation is numerically fulfilled for all cases regardless of the mesh spacing through the face mass fluxes, which is here not shown as no significant plot may be drawn.

However, because of the use of the non-conservative form of the energy equation, the algorithm produces an energy imbalance. To analyse it, the energy Eq. (3) is taken in its steady form and the

convective term as in the r.h.s. of Eq. (18)

$$\rho \frac{\partial h}{\partial t} + \frac{\partial \rho u_j h}{\partial x_j} - h \frac{\partial \rho u_j}{\partial x_j} = \frac{\partial}{\partial x_j} \left(\kappa \frac{\partial T}{\partial x_j} \right) + \frac{dP_o}{dt}, \quad (45)$$

which upon integration over the whole domain (Ω) in

$$\int_{V_\Omega} \frac{\partial \rho u_j h}{\partial x_j} dV_\Omega - \int_{V_\Omega} h_j \frac{\partial \rho u_j}{\partial x_j} dV_\Omega = \int_{A_\Omega} \kappa \frac{\partial T}{\partial x_j} n_j dA_\Omega, \quad (46)$$

where A_Ω and V_Ω denote the domain surface boundaries and volume, respectively. Additionally, the Gauss theorem has been applied to the diffusive term, the term on the r.h.s. of Eq. (46). When the Gauss theorem is applied to the first term on the l.h.s, the integral becomes zero because velocity at boundaries is null. Still, when considering the volumetric integral, numerical errors in the evaluation of the convective term may render it non-null. The divergence of ρu_j should vanish in the steady state. Consequently, the diffusive flux should also go to zero.

However, evaluation of the diffusion heat flux of the converged steady-state results shows that the r.h.s. of Eq. (46) does not exactly vanish. The energy imbalance is caused by the non-conservative part of the convective term, the second term in the l.h.s. of Eq. (46). Numerical integration of this term over the domain is not null, mainly due to evaluation of the mass flux gradients, namely, the divergence of ρu_j . Consequently, heat balance between boundary walls is altered. Notice that this mass flux divergence is not exactly the mass divergence enforced by the continuity equation, but the divergence of a vector field. Thus, numerical errors are introduced by the computation of these gradients at the cell node. In the present work, a least squares procedure is employed to evaluate them [36].

The integral over the domain of the product between the enthalpy and the mass flux divergence, second term on the l.h.s. of Eq. (46), and its reduction as the mesh is refined, is shown in Figure 6. Results are obtained using the collocated discretisation for the momentum equations.

In the figure, it can be seen that the energy imbalance is reduced as the mesh is refined for both schemes. Still, the energy error does not decrease monotonically. The reason for this behaviour are numerical errors in the face interpolations. In this regard, the QUICK scheme is more sensitive to these interpolations because of the intermediate projections required. Although the meshes used in the analysis were created as uniform as possible, non-uniformities and cells with poor geometric

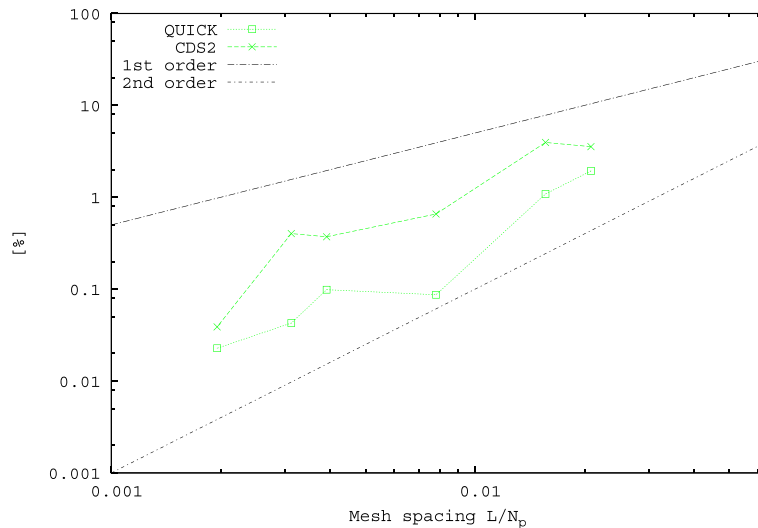


Figure 6. *Test case 2* – Normalised integral over the domain of the product between the enthalpy and the mass flux divergence, corresponding to the second term in the l.h.s. of (46). For comparison, short-dashed-dotted and long-dashed-dotted lines are plotted, showing first-order and second-order convergence rates.

properties, such as high skewness, are still found. Nonetheless, the order of error reduction is close to second order.

In the figure, for the sake of clarity, only the results for the collocated scheme are shown. The reason is that the distinction between collocated and staggered only applies to the momentum equations. Still, simulations were performed to assess possible effects. It is found that the change in discretisation results in minor differences in energy conservation. Because each scheme uses different interpolations for the mass fluxes and velocities, different density fields affect differently each scheme. Nonetheless, as stated, the effect is weak compared with the effect of the face interpolation schemes.

6.2.5. Overall behaviour. Finally, detailed results comparing the CDS2 and QUICK schemes using a mesh spacing of $1/320$ are shown in Table I along with the reference results. For the staggered formulation, only results using the STAGG2 reconstruction method are reported, because the computed values with STAGG1 reconstruction method were not in accordance. It can be seen that the QUICK suffers a deterioration because of the lower-order intermediate interpolations. Furthermore, the QUICK scheme deviates further from the mean at the cold wall. This behaviour is attributable to the fact that the boundary layer is thinner at the cold wall.

Overall, it is observed that the collocated approach offers a computational advantage over the staggered one. The incorrect behaviour of the first-order reconstruction (STAGG1) of the staggered scheme and the higher computational cost of the second-order reconstruction (STAGG2) indicate that the collocated is a more viable approach. Concerning the interpolation schemes, no differences in terms of stability have been observed in the present test case and the general trend for all schemes is similar on unstructured meshes. Still, the QUICK scheme is computationally more expensive because it requires the evaluation of the scalar's gradient. Regarding the accuracy, results obtained using the QUICK scheme show a second-order behaviour. Similarly, the CDS2 performs as a second-order scheme. Nonetheless, with careful observation, it is found a slightly higher order of convergence for the QUICK scheme.

6.3. Test case 3 – Analysis of the transient behaviour

6.3.1. Case definition. The experimental configuration by Markides and Mastorakos [32] is used to test the transient behaviour of the proposed numerical algorithm. This test shows the ability of the proposed scheme to accurately handle and simulate unsteady turbulent flows with variable density, namely, in the low Mach regime, using unstructured meshes. It consists of a fuel jet with a preheated co-flowing air stream, as shown in Figure 7. The co-flowing air is forced to pass through a perforated plate to promote turbulence. The perforated plate (3.0 mm holes and 44% blockage) is located 63 mm upstream of the fuel nozzle to allow turbulence to develop. The fuel nozzle has a diameter of 2.25 mm and is thin walled (0.32 mm). The main test section consists of a 500 mm long and 25 mm inner diameter vacuum insulated quartz tube. The reference experiments were performed over a wide range of operating conditions and four regimes, namely, ‘no ignition’, ‘random spots’, ‘flashback’ and ‘lifted flame’ were identified.

In the present work, the ‘random spots’ regime is simulated, *test case 3*, where auto-ignition kernels appear but are quenched and convected out of the domain before they can act as a flame anchoring point or cause flashback. The fuel is a mixture of H_2 and N_2 ($Y_{H_2} = 0.13$ and $Y_{N_2} = 0.87$) at 750 K and the co-flow oxidiser is air ($Y_{O_2} = 0.233$ and $Y_{N_2} = 0.767$). For the ‘random spots’ regime, the oxidiser temperature is 950 K. Both fuel and air inlet velocities are 26 m/s. The fuel jet Reynolds number is 330, and the co-flow Reynolds number is 5800. The simulation domain spanned from the fuel jet nozzle up to 135 mm in the downstream direction. In order to reproduce the turbulence generated by the perforated plate, an auxiliary non-reactive simulation was performed in an annular mesh, recreating the physical domain upstream to the injector lips. In this non-reacting simulation, the plate was placed inside the domain using the immersed boundary technique. The solution of this non-reactive simulation was then stored and afterwards loaded during the reactive CFD simulation. This method allows a significant saving of computational resources during the numerical simulation and develops a realistic divergence-free velocity field, as opposed to synthetic

turbulence generators based on digital filters. For the fuel jet, a laminar parabolic velocity profile is assumed.

6.3.2. Turbulent formulation. Because the test case here considered is of turbulent nature, the set of transport equations Eqs. (1)–(3), (5) and (6) previously presented have to be formulated in the context of large eddy simulation models using Favre-filtered quantities and closures for the subgrid turbulent fluxes have to be introduced. For the sake of brevity, the equations are not here rewritten, but it is just stated that the variables are Favre-filtered quantities and that in the r.h.s. of the equations, there appears an extra term representing the subgrid turbulent transport. Closure for the momentum turbulent stresses is performed by means of the wall-adapting local eddy-viscosity model [44]. The scalar subgrid turbulent fluxes are modelled using a constant turbulent Schmidt number with value 0.4. The chemical source term is treated explicitly; thus, the filtered reaction terms are assumed to be equal to the reaction rate computed using the filtered quantities $\tilde{w}_k(Y_k, T) = \dot{w}_k(\tilde{Y}_k, \tilde{T})$. The detailed chemical mechanism of Mueller *et al.* [45] is used, which involved 9 species and 21 reactions.

Numerical simulations were performed using a collocated discretisation on a $4 \cdot 10^5$ CV unstructured tetrahedral mesh. Mesh refinement was performed near the air-fuel shear layer and smooth transitions between regions were sought. Given the previous results on the differentially heated cavity, the collocated scheme is used for this test. The decision is justified by the better behaviour of the collocated scheme compared with the staggered scheme using the first-order velocity reconstruction (STAGG1) method (Section 6.2), and the better computational performance of the collocated scheme compared with the staggered scheme using the STAGG2 reconstruction method. Nonetheless, the latter approach yields similar results as the collocated one. Additionally, no mesh refinement was performed because changes in the mesh would modify the effect of the large eddy simulation model.

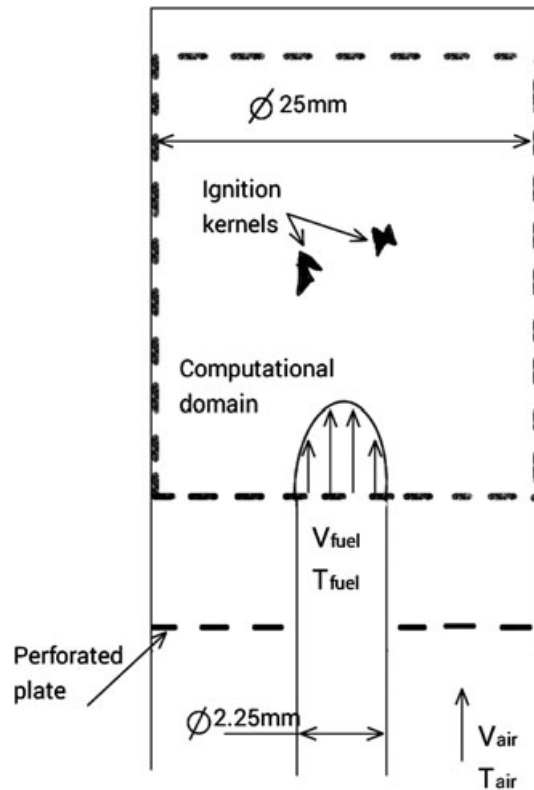


Figure 7. Auto-ignition experimental configuration (test case 3).

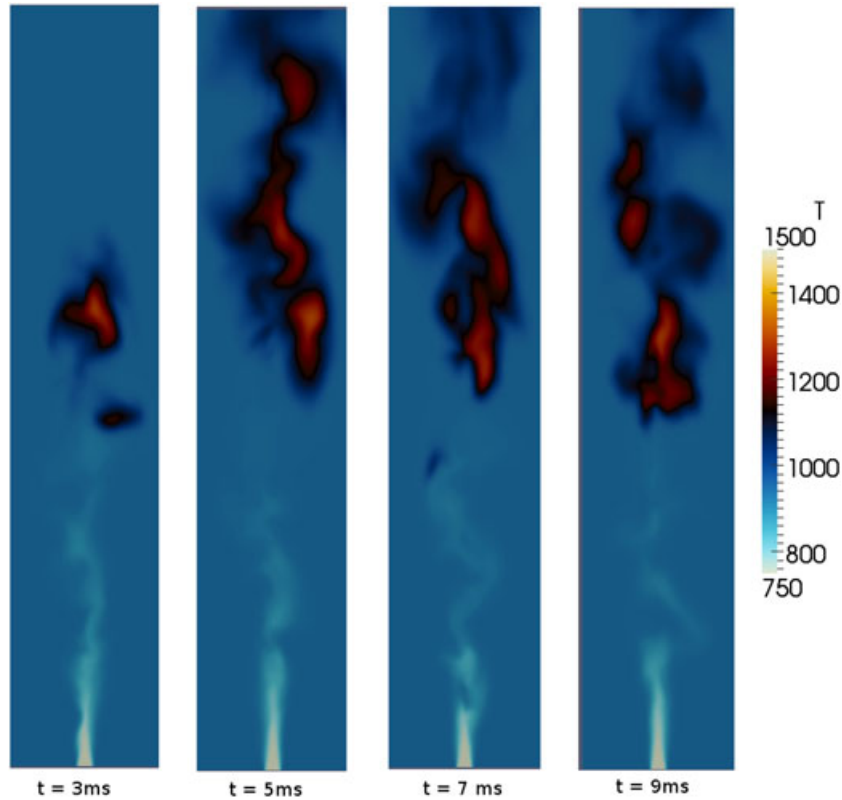


Figure 8. *Test case 3* – Instantaneous snapshots of the temperature. Time scale is adjusted to the beginning of fuel injection ($t = 0$). The axial length of the computational domain is 135 mm. Results are computed using the upwind difference scheme (UDS).

6.3.3. *Transient algorithm analysis.* In the random spots case, the ignition length oscillates around a mean distance from the fuel inlet. This is caused by the appearance of random auto-ignition kernels, which are quenched and convected out of the domain. Several snapshots of the process are shown in Figure 8, where it can be seen that the mixture ignites at different axial locations.

Figure 9 shows the evolution of auto-ignition lengths in time for the random spots regime for different numerical schemes used in the scalar equations. The ignition length is determined using as criterion a rise of 1% in the initial co-flow temperature [46]. Upwinding schemes, namely, the UDS and QUICK scheme, show good agreement with the experimental data. Furthermore, the QUICK is seen to reproduce accurately the experimental data. Explicit treatment of chemical reactions is shown to perform adequately for the current Reynolds numbers. Regarding the CDS2, it features ignition spots at two different heights. One close to the fuel nozzle exit, and another at a higher axial location, which is also shorter than the distance predicted when using the UDS. These ignition kernels are a product of numerical diffusion caused by the numerical scheme, and they do not achieve a temperature high enough to ignite a meaningful quantity of the mixture and stabilise the auto-ignition process at this short distance. The higher axial auto-ignition distances captured by the CDS2, which are similar to those of the upwinding schemes, show where the mixture is actually being completely burned. Comparing the QUICK scheme and UDS, the influence of the numerical diffusivity introduced by the UDS can be seen by the shorter auto-ignition distances predicted by it. Furthermore, when snapshots of the scalar fields are analysed, it is observed that those obtained using the UDS are more blurred compared with those obtained using the QUICK scheme. The reason is that the UDS is a more diffusive scheme, which causes this behaviour.

A final note on computational aspects concerns the stability of the numerical interpolation schemes here used. Initial tests using the QUICK on coarse meshes resulted in unstable simulations because of distorted cells, which were resolved by switching to a UDS. In successive meshes, smooth transitions were sought in order to avoid numerical issues, as in the final mesh whose results

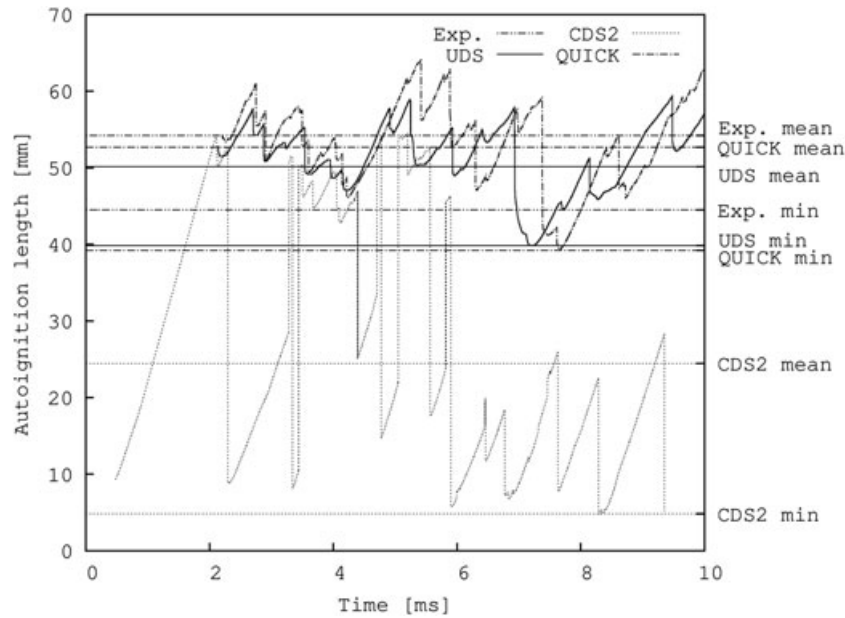


Figure 9. *Test case 3* – Auto-ignition distances for the random spots regime. Horizontal lines represent mean and minimum auto-ignition distances for each numerical scheme and the experimental data. For the latter, only mean and minimum values are plotted.

are here shown. Regarding the momentum equation, no stability issues were detected. Use of the SP scheme resulted in stable simulations.

7. CONCLUSIONS

In this paper, different numerical schemes have been studied to simulate flows in the low Mach regime using unstructured meshes. Focus has been placed on the unstructured discretisation of the equations, concerning numerical interpolations and spatial schemes to handle the pressure-velocity coupling. Two mesh arrangements, collocated and staggered, have been tested. Overall, the proposed numerical algorithm here studied has been shown to be able to accurately and efficiently simulate both laminar and turbulent flows. Tests covered relevant applications of low Mach flows, heat transfer through convection and chemically reacting flows.

Regarding the numerical interpolations, a new approach to define the upwind and downwind nodes of the QUICK interpolation scheme on unstructured meshes has been presented. It has been shown that the scheme has a convergence order higher than second order on structured meshes and is reduced when used on unstructured meshes. However, it is close to second order. This QUICK scheme compared with a second-order centred approximation (CDS2) yields higher errors on coarse meshes. Still, as revealed by the chemically reacting case, centred interpolations, like the CDS2, may introduce numerical artefacts in the computations, which are not observed when using upwind-like schemes. Hence, for cases with high local Peclet numbers, upwind-like schemes are required. Then, the QUICK scheme is preferred over the CDS2 and first-order upwind schemes (e.g. UDS).

Additionally, the SP scheme has been successfully used in the momentum equations in all test cases, showing the suitability of the interpolation scheme to be used for the simulation of low Mach flows.

Concerning the spatial formulations on unstructured meshes, collocated and staggered, extensions have been detailed for their application to low Mach flows. For the staggered scheme, tests have revealed that the first-order reconstruction (STAGG1) method is not suitable for low Mach flows and that the second-order reconstruction (STAGG2) is required. Still, the latter is computationally expensive. Comparatively, the collocated method has shown better behaviour, yielding accurate results with higher computational efficiency.

ACKNOWLEDGEMENT

This study is supported by VAPFLOW – ‘Analysis of mass transfer and phase change phenomena in moist air environments: frosting, defrosting and supersaturated stream mixing’ of the Spanish Government – contract/grant number ENE2012-36910.

REFERENCES

1. Gray D, Giorgini A. The validity of boussinesq approximation for liquids and gases. *International Journal of Heat and Mass Transfer* 1976; **19**:545–551.
2. Choi YH, Merkle C. The application of preconditioning in viscous flows. *Journal of Computational Physics* 1993; **105**(2):207–223.
3. Vierendeels J, Merci B, Dick E. Numerical study of natural convective heat transfer with large temperature difference. *International Journal for Numerical Methods Heat Fluid Flow* 2001; **11**(4):329–341.
4. Kloczko T, Corre C, Beccantini A. Low-cost implicit schemes for all-speed flows on unstructured meshes. *International Journal for Numerical Methods in Fluids* 2008; **58**(5):493–526.
5. Turkel E. Preconditioning techniques in computational fluid dynamics. *Annual Review of Fluid Mechanics* 1999; **31**:385–416.
6. De Sampaio P, Moreira m. a new finite element formulation for both compressible nearly incompressible fluid dynamics. *International Journal for Numerical Methods in Fluids* 2000; **32**:51–78.
7. Becker E, Braack M. Solution of a stationary benchmark problem for natural convection with large temperature difference. *International Journal of Thermal Sciences* 2002; **41**:428–439.
8. Darbandi M, Hosseinizadeh S. General pressure-correction strategy to include density variation in incompressible algorithms. *Journal of Thermophysics and Heat Transfer* 2003; **17**(3):372–380.
9. Lien FS. Pressure-based unstructured grid method for all-speed flows. *International Journal for Numerical Methods in Fluids* 2000; **33**:355–374.
10. Shunn L, Ham F, Moin P. Verification of variable-density flow solvers using manufactured solutions. *Journal of Computational Physics* 2012; **231**:3801–3827.
11. Najm HN, Wyckoff PS, Knio OM. Semi-implicit numerical scheme for reacting flow. I. Stiff chemistry. *Journal of Computational Physics* 1998; **143**:381–402.
12. Kim J, Moin P. Application of a fractional-step method to incompressible Navier–Stokes equations. *Journal of Computational Physics* 1985; **59**(2):308–323.
13. Nicoud F. Conservative high-order finite difference schemes for low-Mach number flows. *Journal of Computational Physics* 2000; **158**:71–97.
14. Knikker R. Comparative study of high-order variable-property segregated algorithms for unsteady low Mach number flows. *International Journal for Numerical Methods in Fluids* 2011; **66**:403–427.
15. Lessani B, Papalexandris M. Time-accurate calculation of variable density flows with strong temperature gradients and combustion. *Journal of Computational Physics* 2006; **212**:218–246.
16. Munz CD, Roller S, Klein R, et al. The extension of incompressible flow solvers to the weakly compressible regime. *Computers and Fluids* 2003; **32**:173–196.
17. Reza Ebrahimi-Kebria1 H, Darbandi M, Hosseinizadeh S. Numerical simulation of low-mach-number laminar mixing and reacting flows using a dual-purpose pressure-based algorithm. *Numerical Heat Transfer, Part B: Fundamentals* 2011; **59**:495–514.
18. Vierendeels J, Rienslagh K, Dick E. A multigrid semi-implicit line-method for viscous incompressible and low-mach-number flows on high aspect ratio grids. *Journal of Computational Physics* 1999; **154**(2):310–341.
19. Vierendeels J, Rienslagh K, Dick E. A multigrid method for all Mach numbers and all grid aspect ratios. *ECCOMAS 2000, Barcelona, Spain, 2000*. CD-rom uitgave, 10 pp.
20. Hall C, Porsching T, Hu P. Covolume-dual variable method for thermally expandable flow on unstructured triangular grids. *International Journal of Computational Fluid Dynamics* 1994; **2**:111–139.
21. Wenneker I, Segal A, Wesseling P. A Mach-uniform unstructured staggered grid method. *International Journal for Numerical Methods in Fluids* 2002; **40**:1209–1235.
22. Vidović D, Segal A, Wesseling P. A superlinearly convergent Mach-uniform finite volume method for the Euler equations on staggered unstructured grids. *Journal of Computational Physics* 2006; **217**:277–294.
23. Mahesh K, Constantinescu G, Moin P. A numerical method for large-eddy simulation in complex geometries. *Journal of Computational Physics* 2004; **197**(1):215–240.
24. Mahesh K, Constantinescu G, Apte S, et al. Large-eddy simulation of reacting turbulent flows in complex geometries. *Journal of Applied Mechanics* 2006; **73**(3):374–381.
25. Felten F, Lund T. Kinetic energy conservation issues associated with the collocated mesh scheme for incompressible. *Journal of Computational Physics* 2006; **215**:465–484.
26. Perot B. Conservation properties of unstructured staggered mesh schemes. *Journal of Computational Physics* 2000; **159**:58–89.
27. Verstappen R, Veldman A. Symmetry-preserving discretization of turbulent flow. *Journal of Computational Physics* 2003; **187**:343–368.

28. Trias F, Lehmkuhl O, Oliva A, Pérez-Segarra C, et al. Symmetry-preserving discretization of Navier–Stokes equations on collocated unstructured grids. *Journal of Computational Physics* 2014; **258**(1):246–267.
29. Jofre L, Lehmkuhl O, Ventosa J, et al. Conservation properties of unstructured finite-volume mesh schemes for the Navier–Stokes equations. *Numerical Heat Transfer, Part B: Fundamentals* 2013; **65**(1):53–79.
30. Pérez-Segarra C, Farre C, Cadafalch J, Oliva A. Analysis of different numerical schemes for the resolution of convection-diffusion equations using finite-volume methods on three-dimensional unstructured grids. Part I: discretization schemes. *Numerical Heat Transfer, Part B: Fundamentals* 2006; **49**:4:351–375.
31. Le Quéré P, Weisman C, Paillère H, Vierendeels J, Dick E, et al. Modelling of natural convection flows with large temperature differences: a benchmark problem for low mach number solvers. Part 1. Reference solutions. *ESAIM: Mathematical Modelling and Numerical Analysis* 2005; **39**(3):609–616.
32. Markides C, Mastorakos E. An experimental study of hydrogen autoignition in a turbulent co-flow of heated air. *Proceedings of the Combustion Institute* 2005; **30**:883–891.
33. Poinot T, Veynante D. *Theoretical and Numerical Combustion*, 3rd Edition. Printed by Aquaprint, Bordeaux, France, 2012.
34. Trias F, Soria M, Pérez Segarra C, Oliva A. A direct Schur–Fourier decomposition for the efficient solution of high-order Poisson equations on loosely coupled parallel computers. *Numerical Linear Algebra* 2006; **13**(4): 303–326.
35. Borrell R, Lehmkuhl O, Soria M, Oliva A. Schur complement methods for the solution of poisson equation with unstructured meshes. *Proc. Par. CFD Conf.*, Antalya, Turkey, 2007; 1–8.
36. Mavriplis DJ. Revisiting the least-squares procedure for gradient reconstruction on unstructured meshes. *16th AIAA Computational Fluid Dynamics Conference*, Orlando, Florida, EE.UU., 2003. NASA CR–2003–212 683.
37. Patankar SV. *Numerical Heat Transfer and Fluid Flow*. Hemisphere Publishing Corporation: Washington - New York - London. McGraw Hill Book Company, New York, 1980.
38. Morinishi Y, Lund T. Fully conservative higher order finite difference schemes for incompressible flow. *Journal of Computational Physics* 1998; **143**:90–124.
39. Rhie C, Chow W. A numerical study of the turbulent flow past an isolated airfoil with trailing edge separation. *AIAA Journal* 1983; **21**:1525–1532.
40. Leonard B. A stable and accurate convective modelling procedure based on quadratic upstream interpolation. *Computer Methods in Applied Mechanics and Engineering* 1979; **19**:59–98.
41. Lehmkuhl O, Pérez Segarra C, Borrell R, Soria M, Oliva A. Termofluids: a new parallel unstructured CFD code for the simulation of turbulent industrial problems on low cost PC cluster. *Proc. Par. CFD Conf.*, Antalya, Turkey, 2007; 1–8.
42. Paillère H, Le Quéré P, Weisman C, Vierendeels J, Dick E, Braack M, Dabbene F, Beccantini A, Studer E, Kloczko T, et al. Modelling of natural convection flows with large temperature differences: a benchmark problem for low Mach number solvers. Part 2. Contributions to the June 2004 Conference. *ESAIM: Mathematical Modelling and Numerical Analysis* 2005; **39**(3):617–621.
43. Trias F, Gorobets A, Oliva. Simple approach to discretize the viscous term with spatially varying (eddy-)viscosity. *Journal of Computational Physics* 2013; **253**:405–417.
44. Nicoud F, Ducros F. Subgrid-scale stress modeling based on the square of the velocity gradient tensor. *Flow, Turbulence and Combustion* 1999; **62**:183–200.
45. Mueller MA, Kim TJ, Yetter RA, Dryer FL. Flow reactor studies and kinetic modeling of the H₂/O₂ reaction. *Int. J. Chem. Kinet.* 1999; **31**(2):113–125.
46. Stanković I, Merci B. Analysis of auto-ignition of heated hydrogen–air mixtures with different detailed reaction mechanisms. *Combustion Theory and Modelling* 2011; **15**(3):409–436.